Journal of Applied Fluid Mechanics, Vol. 12, No. 5, pp. 1463-1473, 2019.
Available online at www.jafmonline.net, ISSN 1735-3645, EISSN 1735-3645.
DOI: 10.29252/jafm.12.05.29705

Study on the Accuracy of RANS Modelling of the Turbulent Flow Developed in a Kaplan Turbine Operated at BEP. Part 2 - Pressure Fluctuations

R. G. Iovănel[1, 2†], G. Dunca[1] and M. J. Cervantes[2]

[1] *University Politehnica of Bucharest, 060042, Romania*
[2] *Luleå University of Technology, 971 87, Sweden*

†*Corresponding Author Email: raluca.iovanel@gmail.com*

(Received October 8, 2018; accepted January 9, 2019)

ABSTRACT

The aim of the paper is to investigate the limitations of unsteady Reynolds-averaged Navier-Stokes (RANS) simulations of the flow in an axial turbine. The study is focused on modelling the pressure pulsations monitored on the runner blades. The scanned blade geometry renders the meshing process more difficult. As the pressure monitor points are defined on the blade surface the simulation relies on the wall functions to capture the flow and the pressure oscillations. In addition to the classical turbulence models, a curvature correction model is evaluated aiming to better capture the rotating flow near curved, concave wall boundaries. Given the limitations of Reynolds-averaged Navier-Stokes models to predict pressure fluctuations, the Scale Adaptive Simulation-Shear Stress Transport (SAS-SST) turbulence model is employed as well. The considered test case is the Porjus U9, a Kaplan turbine model, for which pressure measurements are available in the rotating and stationary frames of reference. The simulations are validated against time-dependent experimental data. Despite the frequencies of the pressure fluctuations recorded on the runner blades being accurately captured, the amplitudes are considerably underestimated. All turbulence models estimate the correct mean wall pressure recovery coefficient in the upper part of the draft tube.

Keywords: Turbulence modelling; Pressure fluctuation; Pressure recovery; Curvature correction; Scale Adaptive Simulation.

NOMENCLATURE

C_{scale}	production correction coefficient	P_w	static pressure at the draft tube wall
Cp_w	pressure recovery coefficient	Q	flow rate
D	runner diameter	R	runner radius
f	frequency	R^*	dimensionless runner radius
k	turbulent kinetic energy	y^+	dimensionless wall distance
P_{w_inlet}	mean static pressure at the draft tube inlet	ρ	fluid density

1. INTRODUCTION

The increasing energy demand and the current trend of continuously expanding sustainable electricity production using renewable energy sources are driving the energy industry to develop new technologies and to reconsider traditional ones. Additionally, the exploitation of intermittent energy resources introduces strong fluctuations to power grids and discontinuities in the provided flow of energy.

Given their flexibility, dimensions and ability to quickly increase or decrease the power output, hydropower plants are able to respond immediately to system disturbances and fast varying loads and demands while maintaining a high efficiency (Bucur *et al.*, 2014). This translates into numerous starts or stops, frequent transient and off-design operations and the need for wider operating ranges for hydraulic turbines. Under these circumstances, hydraulic machines rarely experience steady-state operation. For both the design phase of new

turbines and the rehabilitation of older hydraulic installations, it is mandatory to take into consideration the strong oscillations of the power grid parameters and consequently the transient flows and the real loads (Wylie & Streeter, 1993; Chaudhry, 1987).

Kaplan turbines are double-regulated axial machines i.e. both the angle of the guide vanes and the angle of the runner blades can be adjusted independently. Therefore, Kaplan units have the ability to function efficiently under high load or part load operations compared to the turbines with fixed blades such as Francis or fixed propeller-type turbines. However, frequent off-design operation and the complexity of certain flow conditions, e.g. rotor-stator interaction, high turbulence, may induce varying loads on the runner blades and the bearings.

Numerical simulations have become a powerful tool for understanding flow conditions in different parts of hydraulic systems and turbines (Trivedi, Cervantes & Dahlhaug, 2016; Keck & Sick, 2008). Computational procedures based on numerical methods are being developed and improved in order to provide more and more accurate results (Pinto *et al.*, 2016). Kaplan turbines have been numerically investigated and comparisons with experimental data have been carried out for different analysis models, number of components and turbulence models. Jost, Skerlavaj & Lipej (2014) presented a detailed comparison of both steady-state and unsteady simulations of the flow in a Kaplan turbine. In their study, turbulence models were tested for the steady-state analysis: k–epsilon, k–omega, Baseline (BSL) k-omega model, Shear Stress Transport (SST) all of them improved with the curvature correction (CC) and the Kato-Launder (KL) limiter of turbulence production. The SSG Reynolds stress model was also employed. For the unsteady simulation three turbulence models were used: SST, Scale Adaptive Simulation (SAS) and the Zonal Large-Eddy Simulation (ZLES). The numerical values of the discharge, torque and losses were compared to each other and to measurements. The authors showed that the steady-state analysis failed to predict the flow whereas the unsteady simulations improved the accuracy of the results considerably. Ko & Kurosawa (2014) also presented a numerical simulation of a Kaplan turbine. They used the Reynolds Stress turbulence Model (RSM) and the results were compared with those of a Large-Eddy Simulation (LES). As opposed to the LES, the RSM simulation numerically damped the blade tip vortex. The pressure fluctuations at the runner outlet were therefore underestimated. Wu *et al.* (2012) considered the hub clearance flow in a Kaplan turbine using an SST steady-state simulation. The authors presented the pressure distribution on the suction side of the blade and found that the front hub clearance has a limited influence on the flow whereas the rear hub clearance reduces the pressure considerably near the hub and shroud.

Studies involving numerical simulations that capture the pressure variation in different parts of the turbine are not frequently encountered in the literature. Liu *et al.* (2008, 2009) investigated pressure fluctuations in particular using an unsteady simulation of the complete flow passage in a Kaplan turbine model and prototype. The predicted oscillations were compared to experimental measurements in the distributor, below the runner blades and in the draft tube cone and draft tube elbow. The simulated values were found in good agreement with the experimental ones with some exceptions for two draft tube sections. More recently, Wu *et al.* (2011) simulated the unsteady flow through the entire passage of a Kaplan prototype turbine using an unsteady Reynolds-averaged Navier-Stokes (URANS) simulation and several turbulence models: k-omega, SST and RNG k-epsilon. They analyzed the pressure fluctuations in seven different locations: three upstream the runner and four downstream. At the section located just below the trailing edges of the blades, the first frequency peak was a low frequency given by the upstream propagation of the vortex rope pulsation. The second peak was found at the runner rotating frequency. The frequency and amplitude of the pressure fluctuations in the prototype were compared to those obtained in the model for both on-cam and off-cam operations. The relative frequencies of the pressure fluctuations were similar for the model and the prototype, except for the low values.

Other numerical investigations of Kaplan turbines were performed by Luo *et al.* (2013) for eight different operating points. Their study showed that the vortices in the vaneless space between the distributor and the runner cause large pressure pulsations. They also found that the frequencies and amplitudes of the dynamic stresses in the runner body strongly influence the pressure pulsations on the blades. Zhou *et al.* (2007) focused on the dynamic stresses in Kaplan blades. They presented pressure distributions on the blades and pressure fluctuations on the suction and pressure side of one blade for multiple operating conditions.

Mulu *et al.* (2015) numerically studied the flow in the Kaplan turbine model, Porjus U9. The computational domain included the full guide vanes, runner and draft tube. Different turbulence models were tested: k-epsilon, RNG k-epsilon, SST and SAS-SST. The unsteady simulation was validated against velocity and pressure measurements performed in the draft tube. The wall pressure recovery (Cp_w) of the draft tube conical diffuser was obtained both numerically and experimentally and compared at four different angular positions. It was shown that all turbulence models accurately predicted the pressure recovery with some differences at the sections closest to the draft tube elbow. However, the axial velocity profile was not correctly predicted just below the runner cone, after the draft tube inlet Because the runner-draft tube interface was located right after the trailing edges of the blade, it is possible that the blade wakes were mixed and dissipated.

Pressure fluctuations on the Porjus U9 runner blades were numerically investigated by Amiri *et al.* (2016a). An unsteady simulation was performed

using the SAS-SST model. The numerical model included the spiral casing, the distributor featuring 18 stay vanes and 20 guide vanes, the runner and the draft tube. The authors explored the influence of the boundary conditions at the inlet of the spiral casing over the prediction of the pressure fluctuations exerted on the runner blades. The authors showed that the dominant frequencies in the amplitude spectra were accurately estimated. The runner rotational frequency had the highest amplitude. Possible justifications for this fact were a supposed perturbation in the water supply system, asymmetry in the distributor or the effects of the draft tube downstream the runner. The numerically determined amplitudes represented however, only a third of the amplitudes obtained experimentally.

The current paper presents unsteady numerical simulations of the flow in the Porjus U9 Kaplan turbine model focusing on the sources of asymmetric hydraulic loads present in the runner at the best efficiency operating point (BEP) and their periodicity. Four turbulence models have been tested: k-epsilon, RNG k-epsilon SST and SAS-SST. The curvature corrected SST model (SST-CC) proposed by Smirnov & Menter (2009) is also used, in the attempt to better predict the complex three dimensional rotating flow. The simulations are employing the production correction coefficient C_{scale} = 1 and a second value of 1.25 corresponding to strong concave curvature and enhanced turbulence production. The unsteady SAS-SST simulation is performed in order to better resolve the turbulent structures. The SAS-SST turbulence model allows the formation of a more detailed turbulence spectrum and therefore is expected to be more accurate than RANS models while remaining computationally efficient and fast (Menter & Egorov, 2010). The computational domain includes the entire distributor, runner and draft tube. The numerical values are compared to pressure measurements performed on two consecutive blades and in the draft tube cone. The draft tube pressure recovery coefficient is also presented. The pressure fluctuations exerted on the blades of the Kaplan turbine model are investigated in order to identify potential sources of asymmetric loads on the rotating parts of the turbine.

2. TEST CASE

The Porjus U9 turbine is the 1:3.1 scaled model of the Kaplan prototype located in Porjus, Sweden. A detailed description of the test rig and model is presented by Mulu *et al.* (2012). The diameter of the model runner is D = 0.5 m. The net head is 7.5 m and the runner rotational speed is 696.3 rpm. At BEP the guide vane angle is 26.5º and the corresponding mass flow rate is 690 kgs^{-1}.

Mulu *et al.* (2012) performed an extensive experimental study of the flow in the draft tube of the aforementioned model at the BEP and two off-design operating points (Jonsson, Mulu & Cervantes, 2012). Combining Laser Doppler Anemometry (LDA) and flush mounted pressure sensors, the authors focused on the influence of the swirl leaving the runner. The blade wakes were visible only in the upper part of the cone. The pressure recovery was high in the draft tube cone (70%), decreased near the elbow and increased again in the outlet diffuser.

Twenty equally distanced pressure taps were installed on the draft tube cone walls at four angular positions a, b, c and d with 90º spacing around the circumference. The sensors locations are shown in Fig. 1. The accuracy of the pressure transducers was reported at 0.1%. In this paper, the pressure monitor points are numbered P1-P5 starting from the top.

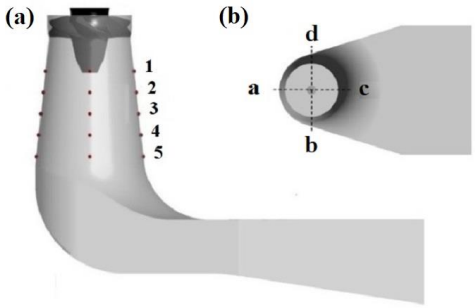

Fig. 1. U9 draft tube and pressure sensors locations. (a) Red dots mark the pressure taps numbered P1 to P5 starting from the top. (b) Circumferential positions for the pressure measurements.

Another measurement campaign, involving the same Kaplan model was performed by Amiri *et al.* (2015), this time focusing on the turbine runner. At BEP, the measurements showed that an asymmetric flow was delivered to the guide vanes close to the lip entrance junction resulting in flow separation. The wakes of the guide vanes were propagating downstream, therefore inducing large pressure fluctuations on the runner blades. Unsteady pressure measurements were also carried out during load acceptance and load rejection, on the blades and draft tube walls of the Porjus U9 model (Amiri, Mulu, Raisee & Cervantes, 2016a). The purpose of this experimental investigation was to monitor the formation and mitigation process for the rotating vortex rope and their influences on the forces wielded on the runner blades.

Twelve pressure sensors were installed on the pressure and suction side of two consecutive blades. The sensors located on the pressure side of blade 1 are labelled PS1 to PS6 and the sensors installed on the suction side of blade 2, SS1 to SS6. The signals from all the sensors were simultaneously recorded at a constant sampling frequency of 4 kHz. The location of the pressure sensors are presented in Fig. 2.

Soltani *et al.* (2015) discussed the pressure measurements performed on the runner blades of the model showing that different regions of the blade become critical at different operating points. As expected, the amplitude of pressure fluctuations recorded on the blades was larger during the transient operations.

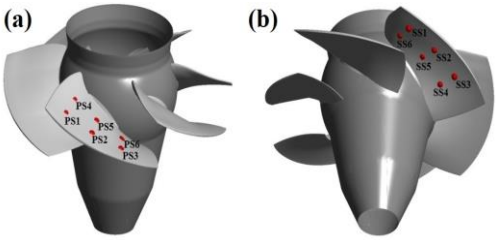

Fig. 2. U9 runner and pressure sensors locations. (a) Pressure sensors placed on the pressure side of blade 1. (b) Pressure sensors placed on the suction side of blade 2.

3. NUMERICAL CASE

The reported calculations were performed using ANSYS CFX 16.2. Unsteady simulations are performed for the entire turbine assembly. Transient Rotor-Stator interfaces are defined between the three domains: guide vanes, runner and draft tube. A steady-state simulation using the Frozen Rotor interface is used to provide the initial values.

The computational flow domain included the full guide vane composed of 20 identical blades, the runner domain with 6 runner blades and the draft tube, see Fig. 3. The runner blade was scanned using a 3D optical scanning device (ATOS III system from GOM) and the geometry included the hub and tip clearances of the runner blade. Only one blade passage was modelled for the guide vanes and the runner. The mesh was then copied and rotated to ensure axial symmetry in these two domains. The draft tube domain was extended at the outlet with a 2m straight channel.

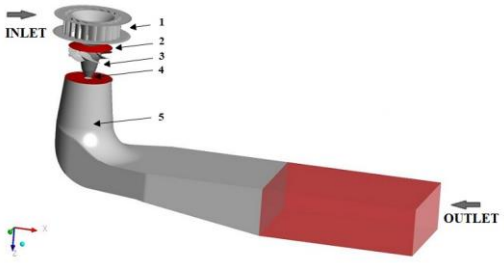

Fig. 3. Computational domains: 1. Guide vane domain. 2. Guide vane-Runner interface. 3. Runner domain. 4. Runner-Draft tube interface. 5. Draft tube domain.

The hexahedral mesh generated for all three domains is created in ICEM 16.2 (Fig. 4). The lowest value for the minimum orthogonal angle is 16.8º reached in the runner domain and the maximum exponential factor was 48, also in the runner. The total number of cells in the entire domain is 10.39×10^6. The mesh properties evaluated by CFX are presented in Table 1.

In the guide vane domain, the y^+ values are smaller than 165 whereas in the runner, they are kept below 235. In the draft tube domain y^+ is smaller than 5.

Only locally (in the clearances), the y^+ values are larger than the requirements of the turbulence models and the wall functions are employed. In order to meet the y^+ criteria, a very fine mesh is required, considerably increasing the computational demands and the total simulation time. A mesh sensitivity analysis was presented by Mulu *et al.* (2015). However, the runner mesh created for the present numerical model is coarser due to the use of the scanned blade geometry.

Table 1 Quality parameters of the mesh

Domain	Minimum angle [º]	Expansion factor	Aspect ratio
Guide vane	19.9	21	84
Runner	16.8	48	668
Draft tube	30.5	9	7635

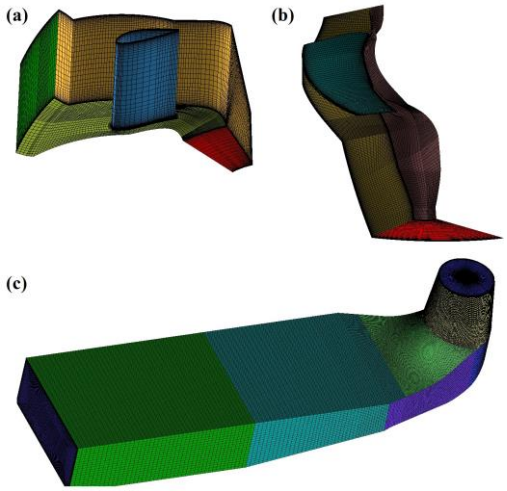

Fig. 4. Porjus U9 mesh. (a) guide vane. (b) runner blade. (c) draft tube.

The specified boundary conditions were the inlet mass flow of 690 kg/s at the flow angle of 30º as it is provided at the spiral casing outlet, smooth walls with the no-slip condition imposed and the outlet boundary condition which was set as zero average static pressure.

Several two-equation RANS turbulence models have been tested: k-epsilon and RNG k-epsilon, using the scalable wall function and SST using the automatic wall function. Also, two simulations have been run with the curvature corrected SST turbulence model, for two different values of the production correction coefficient C_{scale}. RANS turbulence models employ a statistical representation of the turbulence. The Boussinesq hypothesis relating the turbulent stresses to the mean flow with the help of the turbulent eddy-viscosity, characterizes such models. These turbulence models are dissipative, because of the increased viscosity, and are unable to properly capture flow structures generated by normal Reynolds stress anisotropies (Alfonsi, 2009).

The time step or sampling resolution in a time dependent simulation is chosen by considering the smallest frequency of the system to be resolved.

The sampling resolution frequency should be at least ten times smaller than the frequency that characterizes the phenomena for a good resolution, i.e., at 10 points to resolve a sinusoid. If the sampling resolution frequency corresponding to the time step falls in the turbulence spectrum, the unsteady terms of the Reynolds equations will resolve part of the turbulence, from the lowest frequency to half the resolution sampling frequency according to the Nyquist criteria. As part of the turbulence is resolved, an overestimation of the turbulent viscosity may arise leading to a damping of these fluctuations to be resolved (Wilheim, 2016). Therefore, the diffusive character of RANS models may lead to a strong damping of fluctuations in the flow parameters.

Because the pressure fluctuations captured with these turbulence models had very small amplitudes, the SAS-SST turbulence model has also been used in this study. The SAS-SST turbulence model is an improved URANS model that can adjust the length scale to the resolved turbulence scale. SAS-SST is smoothly transitioning from a LES turbulence model through several eddy scales to the steady RANS modelling.

All computations were performed using a high resolution scheme for the advection term. For the unsteady simulation, a second order backward Euler scheme was used to solve the time dependent term in the Reynolds equations. The transient time step was set to 4×10^{-4} s, corresponding to 1.67º of the runner revolution.

The simulations were converged and then run for three full rotations for each RANS turbulence model investigated: k-epsilon, RNG k-epsilon, SST, SST-CC with a correction coefficient C_{scale} = 1 and SST-CC with a correction coefficient C_{scale} = 1.25. Although the SAS-SST simulation was converged in the residuals and the value of the maximum residual for each equation solved was below 10^{-4}, the monitor points showed no periodic variation of the recorded variables.

4. RESULTS AND DISCUSSIONS

The pressure values are extracted from the CFD simulations using 32 monitor points: 12 monitor points defined on two consecutive blades and 20 monitor points defined around the draft tube cone at the same locations as the pressure sensors (Figs. 1 and 2).

The time averaged pressure values on the runner blades are made dimensionless with respect to the turbine operational head and compared to the experimental values determined by Amiri *et al.* (2015). The amplitude spectra of pressure signals from the monitor points located on the suction and pressure sides of the runner blades are evaluated for all turbulence models The frequencies are made dimensionless using the rotating frequency of the turbine f_{runner} = 11.61 Hz.

The draft tube pressure recovery coefficient is calculated based on the wall pressure simulated in the draft tube cone, as it is determined by Mulu *et al.* (2012):

$$Cp_W = \left(P_W - P_{W\_inlet}\right) \Big/ \frac{\rho}{2}\left(\frac{Q}{A_{inlet}}\right)^2 \quad (1)$$

where P_w is the pressure along the draft tube cone, P_{w_inlet} is the pressure recorded experimentally or numerically at position P1 (Fig. 1), A_{inlet} is the draft tube cross-sectional area at the same position and Q is the flow rate.

All geometric dimensions are made dimensionless relative to the runner radius R = 0.25 m.

4.1 Runner Blades

The time averaged pressure values obtained from the numerical simulations show no sensitivity to the turbulence models. Comparisons between the numerically calculated values and the experimental values are presented in Fig. 5. All simulations show an underestimation of the pressure on both the pressure and the suction sides of the runner blade. The only exception is noticed at the location of pressure sensor PS1, located on the pressure side of the runner blade, near the leading edge.

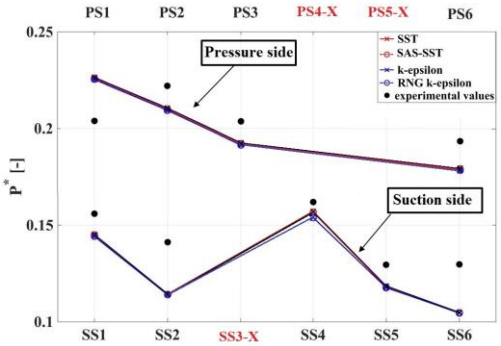

Fig. 5. Experimental and simulated pressure values on the runner blade.

Each simulation was performed for three complete runner rotations. The pressure values were recorded by 32 monitor points defined at the pressure taps location. Each monitor point provides pressure values $p(t)$ that can be decomposed into three components: the time average $\bar{p}$, periodic oscillations $\tilde{p}(t)$ and random fluctuations $p'(t)$. Thus, the phase averaged profile $\langle p(t) \rangle$ is defined by:

$$\langle p(t) \rangle = \bar{p} + \tilde{p}(t) = p(t) - p'(t) \quad (2)$$

Figure 6 presents an example of the phase averaged pressure over one runner revolution. Due to the chosen time step of 4×10^{-4} s, the pressure values are not calculated at the same location. The time step corresponds to a runner rotation of 1.67º therefore the calculated pressure values are not identical for all runner rotations. The guide vane wakes visible in Fig. 6 are changing in amplitude due to different harmonics that interfere. The pressure fluctuations amplitudes will be discussed individually for each

turbulence model.

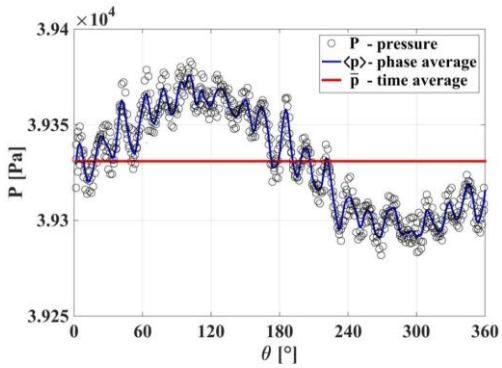

Fig. 6. Phase averaged pressure over one runner revolution, $\Delta\theta$=1.67°. Results are presented for the RNG k-epsilon turbulence model, pressure sensor PS2 on the pressure side of the runner blade.

As mentioned before, two values of the production multiplier C_{scale} are employed in the present paper for the curvature corrected SST turbulence model. According to Smirnov & Menter (2009) the larger values correspond to a strong concave curvature. In the CFX solver, the standard value is C_{scale} = 1. However, when looking at the pressure fluctuations, the two corrections show virtually identical results with the classical SST model. Therefore, out of the three SST simulations, only the results of the latter are presented. The SAS-SST simulation did not record periodic fluctuations at the monitor point locations, although the unsteady solution was converged with the value of the root mean square (RMS) residuals of 10^{-4}.

The pressure measurements presented by Amiri *et al.* (2015) showed large pressure oscillations corresponding to the runner frequency and the guide vane passing frequency. The authors concluded that the pressure fluctuation peaks at the runner rotational frequency were caused by a perturbation in the water supply system, the effects of the draft tube elbow downstream the runner, or a mass imbalance in the rotating parts of the turbine.

The inlet boundary condition for the numerical model investigated in the current paper is a symmetrical, uniformly distributed mass flow rate specified upstream the guide vanes. The mesh and geometry for all guide vanes are identical. The six runner blades are identical as well. Therefore, there is no asymmetry expected in the flow provided to the runner as shown in Fig. 7.

Figure 8 presents the amplitude spectra of the pressure variation recorded by the monitor points located on the pressure and suction sides of the runner blades. The figure shows the results at the monitor points that correspond to the sensors placed near the shroud of the runner. The monitor point PS1 is located near the leading edge and PS3, near the trailing edge of the pressure side of the blade. On the suction side, results are presented for the corresponding sensors SS1 and SS3 as seen in Fig. 2. The other monitor points located near the runner hub showed similar results.

The results are presented for four turbulence models: SST, k-epsilon, RNG k-epsilon and SAS-SST. All models show amplitude peaks at the runner rotational frequency f_{runner}, guide vane passing frequency, 20 f_{runner} and two small amplitude spikes at 12 f_{runner} and 18 f_{runner}. These two peaks should correspond to lower harmonics of pressure fluctuations given by the runner blades passing, 6 f_{runner}. The RNG k-epsilon turbulence model captures the highest pressure fluctuations, followed by the classical k-epsilon model. The SST model provides small amplitude especially at low frequencies. As expected, the SAS-SST simulation captures very small amplitudes of the fluctuations because the monitor points did not record periodic pressure variations.

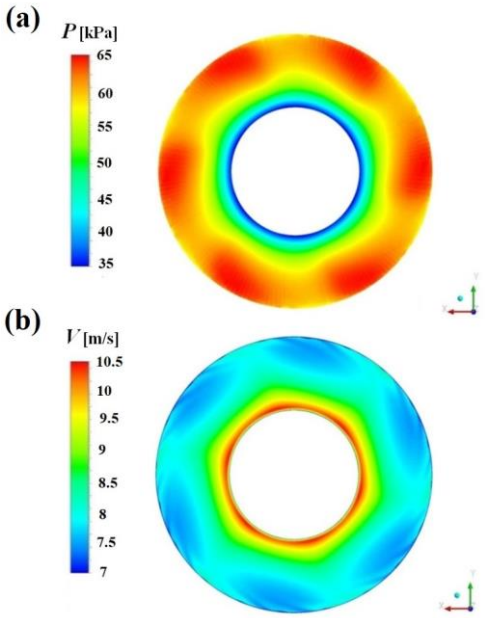

Fig. 7. Pressure (a) and velocity (b) contours at the runner inlet section. Results are presented for the RNG k-epsilon turbulence model.

In all simulations, the dominant frequency of the pressure oscillations is the runner rotational frequency f_{runner}. The amplitude spectra of the numerically obtained pressure signal on the pressure side of the blade at the runner frequency are shown in Fig. 8a and 8c and present significantly smaller pressure amplitudes when compared to the spectra calculated for the suction side of the blade, Fig. 8b, 8d. This is expected because, as stated before, the flow domain upstream the runner is axisymmetric and there is no perturbation that should cause fluctuations on the pressure side of the blades at the runner frequency.

The only possible cause should be an asymmetry in the runner downstream geometry, specifically the draft tube elbow since it is also the only asymmetric feature of the model. This is confirmed by the

amplitude spectra presented in Fig. 8. The highest peak is found at the monitor point corresponding to pressure sensor SS3, located near the trailing edge of the blade and the amplitude is decreasing towards the leading edge at monitor point SS1.

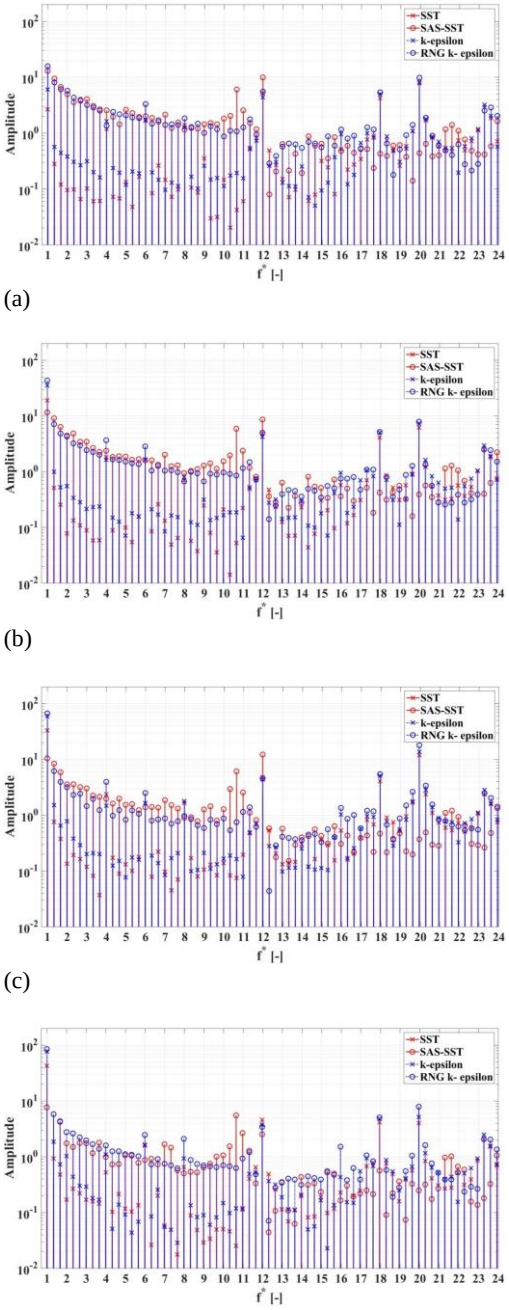

Fig. 8. Amplitude spectra of the pressure sensor signals on the pressure side of the blade: (a) PS1, (c) PS3 and on the suction side of the blade: (b) SS1, (d) SS3.

For pressure sensors PS1 and SS1, which are closest to the leading edge, another peak can be observed at the dimensionless frequency 20 f_{runner} corresponding to the guide vane wakes. Downstream, the amplitude of the pressure fluctuations given by guide vanes is rapidly decreasing. As expected, the values are smaller on the suction side. Additionally, compared to the measurements, the amplitude corresponding to the guide vane passing frequencies are considerably smaller. This is most probably due to the dissipative character of URANS turbulence models. The guide vane trailing edge wakes propagating downstream are spread out and damped.

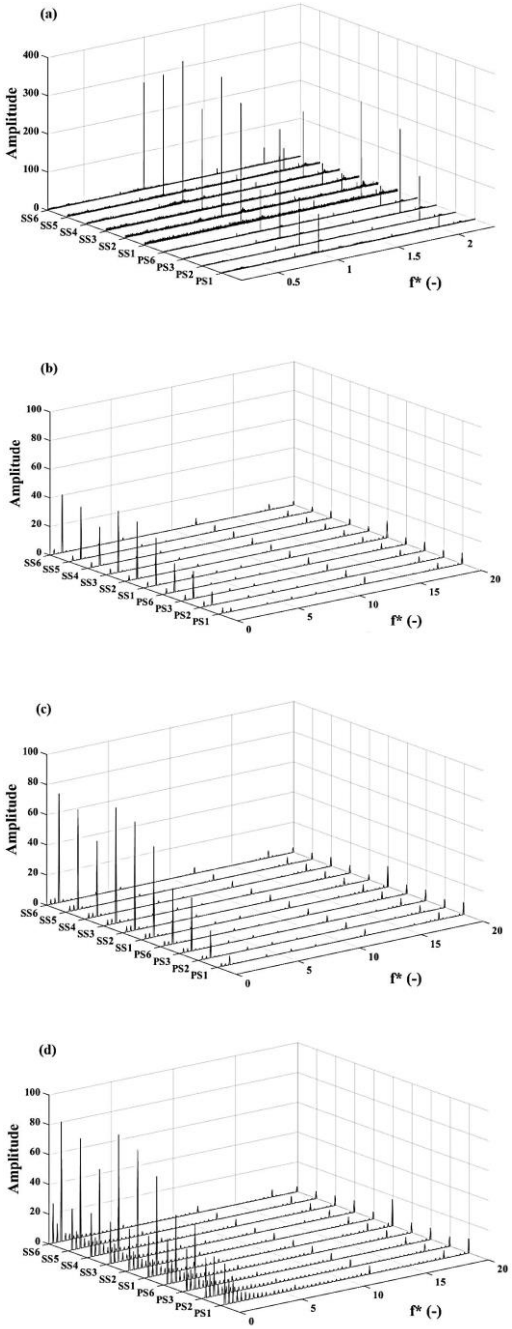

Fig. 8. Waterfall plots of the pressure signals monitored on the runner blade: (a) experimental results from Amiri *et al.* (2015), (b) CFD simulations, SST turbulence model, (c) CFD simulations, k-epsilon turbulence model and (d) CFD simulations, RNG k-epsilon turbulence model.

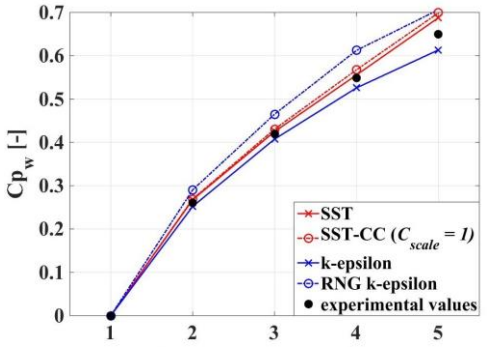

(a)

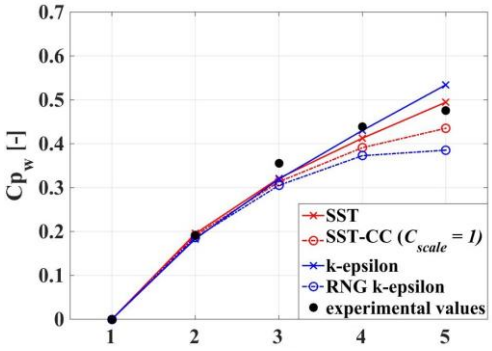

(b)

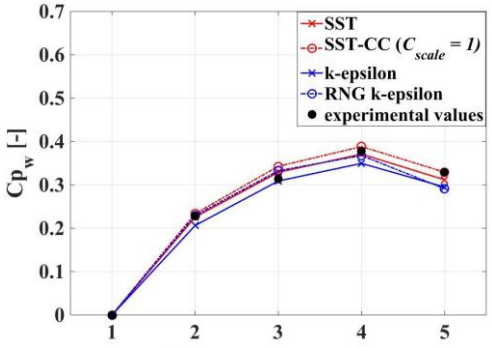

(c)

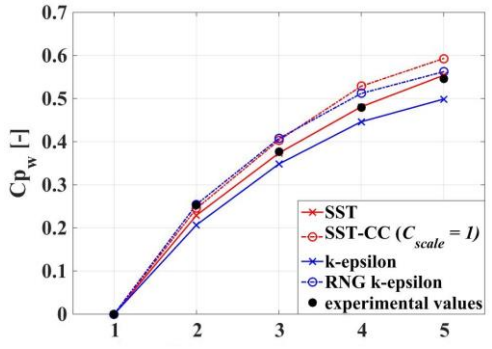

(d)

Fig. 9. Wall pressure recovery factor of the draft tube conical diffuser, Cp_w, obtained experimentally and numerically at: (a) angular position a, (b) angular position b, (c) angular position c, (d) angular position d. (see Fig. 1).

Figure 8 presents waterfall plots of the pressure signals obtained from all the monitor points on the runner blades from the numerical simulations using the SST, k-epsilon and RNG k-epsilon turbulence models (Fig. 8b-8d) compared to the experimental results obtained by Amiri *et al.* (2015) (Fig. 8a). The dominant dimensionless frequencies are 1 f_{runner} and 20 f_{runner}, corresponding to the runner rotation and the guide vane passing frequencies. Because all the harmonics of f_{runner} are present in the spectrum, only the low frequencies are presented in Fig. 8a. The results obtained using the SAS-SST turbulence model were excluded because, as stated before, the simulation provided very small amplitudes especially at low frequencies.

The results show that the frequencies are accurately predicted by the numerical simulations as opposed to the corresponding amplitudes. The experimental amplitude values are larger by a factor of 5 to 6 depending on the sensor position.

Both turbulence models show a downstream increase of the pressure amplitude peaks at the runner rotational frequency. The highest pressure fluctuations corresponding to the runner frequency are obtained near the trailing edge of the blade (monitor points SS3 and SS6) whereas the lowest are obtained near the leading edge (monitor points SS1 and SS4). The results suggest that the runner frequency of f_{runner} is present in the blade pressure amplitude spectra due to the draft tube elbow downstream the runner.

The simulated guide vanes passing frequency is very small compared to the experimental values regardless of the turbulence model. To some extent this is an expected outcome given the limitations of RANS models.

4.2 Draft Tube

The wall pressure recovery coefficient of the conical diffuser is calculated according to Eq. 1 using the numerically predicted pressure values recorded at the monitor points (Fig. 1) and the experimental data provided by Mulu *et al.* (2012).

Figure 9 presents the pressure recovery factor at four angular positions, obtained experimentally and numerically using three different URANS turbulence models and the curvature corrected SST model. The draft tube wall pressure recovery is defined as the ratio of the pressure difference between the section of interest and the draft tube inlet to the dynamic pressure based on the mean axial velocity at the inlet section. This factor is used to evaluate the performance of the draft tube as it quantifies the amount of kinetic energy recovered along the draft tube.

As the flow decelerates towards the back of the draft tube (outer radius), the static pressure increases. The opposite situation is encountered at the inner draft tube radius where the flow is accelerated and the static pressure decreases. As a consequence, the highest pressure recovery is found at the angular position (a) both experimentally and numerically. At the angular position (c), the lowest pressure recovery is predicted.

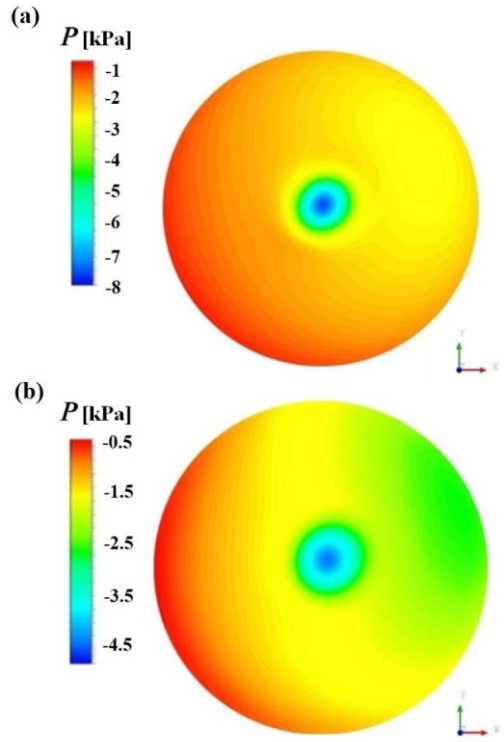

Fig. 10. Pressure contours in the draft tube cone: pressure sensors 4-a to 4-d (left) and pressure sensors 5-a to 5-d (right). Results of the SST-CC simulation.

All turbulence models show good agreement with the experimental data. At sections (a) and (d) the pressure recovery factor is overestimated near the draft tube elbow. The SST turbulence model and the SST-CC using the production multiplier C_{scale} = 1 show the best results. The curvature correction reduces the eddy-viscosity (Smirnov & Menter, 2009) therefore the model is able to better capture the secondary flows at the last two sections, 5 and 4, just above the draft tube elbow. The k-epsilon and RNG k-epsilon turbulence models show a slightly larger overestimation of Cp_w.

At the angular positions (b) and (c) the turbulence models behave in a similar manner but the pressure recovery coefficient is underestimated. The SST simulations capture the pressure recovery accurately and match the experimental results with very small differences. The k-epsilon turbulence models provide the largest discrepancies between numerical and experimental values.

The flow downstream the draft tube elbow is considered similar to the flow after a 90° pipe bend, therefore secondary flow after the draft tube bend is induced by centrifugal forces. The measurements presented by Amiri *et al.* (2016b) showed that the swirl at the draft tube inlet is influencing the flow in the straight diffuser. The numerical simulations underestimate the tangential velocity and as a consequence, the two counter rotating vortices after the draft tube bend are nearly symmetrical. However, the experiments show a larger flow asymmetry because the vortex co-rotating with the upstream swirl is stronger.

Figure 10 presents the pressure contour plots obtained from the simulation using the SST-CC turbulence model with the maximum value of the production coefficient at the two lowest sections of the draft tube cone corresponding to positions P4 and P5 (before the bend). The pressure distribution is axisymmetric in the upper part of the draft tube cone where the first three locations of the pressure sensors are. Further downstream, in the vicinity of the draft tube elbow, the pressure contour plots show an asymmetric low pressure area in the front part of the draft tube. The pressure distribution is in agreement with the predicted pressure variations obtained by Liu, Li & Wu (2009).

5. CONCLUSIONS

Unsteady simulations were carried to investigate the turbulent flow developed inside a Kaplan turbine model at BEP. The k-epsilon, RNG k-epsilon and SST turbulence models were tested. Simulations were also performed for the curvature corrected SST turbulence model using the standard recommended value of the production correction coefficient C_{scale} = 1, and a higher value, C_{scale} = 1.25 corresponding to a strong curvature. Additionally, a simulation using the SAS-SST turbulence model was performed. The numerical domain included the complete guide vanes, the runner and the draft tube.

The time averaged pressure values recorded by the monitor points defined on the runner blades were compared to the experimental results. The results showed that the numerical model is insensitive to the turbulence models and in good agreement with the measurements.

The pressure fluctuations on the pressure and suction sides of the blades were investigated. The frequencies were accurately captured but the corresponding amplitudes were underestimated by a factor of approximately 5÷6 regardless of the turbulence model.

The largest amplitudes of the pressure fluctuations corresponded to the runner rotational frequency of f_{runner} and were recorded on the suction sides of the blades. The results showed that the maximum amplitudes were obtained near the trailing edge of the runner blades, closest to the draft tube. Therefore, a possible source for the asymmetric loads present in the runner at BEP is the draft tube elbow and its influence on the upstream flow. Such asymmetric loads affect the runner blades, the shaft and bearing, reducing their lifetime and the quality of their performance.

The numerical wall pressure recovery results were very similar to the experimentally obtained values. The best agreement was provided by the SST simulation and the SST-CC.

The SAS-SST simulation was expected to capture higher pressure fluctuations at the monitor points defined on the blade surface. However, the

computations showed poor convergence in the monitor points and the pressure signal could not be processed like it was done for the RANS simulations.

A mesh sensitivity analysis is required at least for the turbulence models that performed best, in order to better resolve the boundary layer and to predict accurately the pressure fluctuations inside the Kaplan model.

ACKNOWLEDGEMENTS

The research presented was carried out as a part of "Swedish Hydropower Centre – SVC." SVC was established by the Swedish Energy Agency, Elforsk and Svenska Kraftnät together with the Luleå University of Technology, The Royal Institute of Technology, Chalmers University of Technology and Uppsala University (www.svc.nu).

REFERENCES

Alfonsi, G. (2009). Reynolds-averaged Navier-Stokes equations for turbulence modelling. *Applied Mechanical Reviews* 62(4).

Amiri, K. (2016). *Effects of upstream flow conditions on runner pressure fluctuations*. Ph.D. thesis, Lulea University of Technology, Lulea, Sweden.

Amiri, K., B. Mulu, M. Raisee and M. J. Cervantes (2016b). Experimental study on flow asymmetry after the draft tube bend of a Kaplan turbine. *Advances and Applications in Fluid Mechanics* 19(2), 441-472.

Amiri, K., B. Mulu, M. Raisee and M. J. Cervantes (2016a). Unsteady pressure measurements on the runner of a Kaplan turbine during load acceptance and load rejection. *Journal of Hydraulic Research* 54(1), 56-73.

Amiri, K., M. J. Cervantes and B. Mulu (2015). Experimental investigation of the hydraulic loads on the runner of a Kaplan turbine model and the corresponding prototype. *Journal of Hydraulic Research* 53(4), 452-465.

Bucur, D. M., G. Dunca, M. J. Cervantes, C. Călinoiu and E. C. Isbăşoiu (2014). Simultaneous transient operation of a high head hydro power plant and a storage pumping station in the same hydraulic scheme. *IOP Conference Series: Earth and Environmental Science* 22(4).

Chaudhry, M. H. (1987). *Applied Hydraulic Transients*. Van Nostrand Reinhold Company, New York, USA.

Jonsson, P., B. Mulu and M. J. Cervantes (2012). Experimental investigation of a Kaplan draft tube - Part II: Off-design conditions. *Applied Energy* 94, 71–83.

Jost, D., A. Skerlavaj and A. Lipej (2014). Improvement of Efficiency Prediction for a Kaplan Turbine with Advanced Turbulence Models. *Journal of Mechanical Engineering* 60(2), 124-134.

Keck, H. and M. Sick (2008). Thirty years of numerical flow simulation in hydraulic turbomachines. *Acta Mechanica*201, 211–229.

Ko, P. and S. Kurosawa (2014). Numerical simulation of turbulence flow in a Kaplan turbine - Evaluation on turbine performance prediction accuracy. *IOP Conference Series: Earth and Environmental Science* 22.

Liu, S., J. Shao, S. Wu and Y.L. Wu (2008). Numerical simulation of pressure fluctuation in Kaplan turbine. *Science in China Series E: Technological Sciences* 55(8), 1137–1148.

Liu, S., S. Li and Y. Wu (2009). Pressure Fluctuation Prediction of a Model Kaplan Turbine by Unsteady Turbulent Flow Simulation. *Journal of Fluids Engineering* 131(10).

Luo, Y., Z. Wang, J. Zhang, J. Zeng, J. Lin and G. Wang (2013). Vibration and fatigue caused by pressure pulsations originating in the vaneless space for a Kaplan turbine with highhead. *Engineering Computations* 30(3), 448 – 463.

Menter, F.R. and Y. Egorov (2010). The Scale-Adaptive Simulation Method for Unsteady Turbulent Flow Predictions. Part 1: Theory and Model Description. *Flow Turbulence and Combustion* 85(1), 113-138.

Mulu, B., M. J. Cervantes, T. Vu, C. Devals and F. Guibault (2015). Simulation-based investigation of unsteady flow in near-hub region of a Kaplan turbine with experimental comparison. *Engineering Applications of Computational Fluid Mechanics* 9(1), 139-156.

Mulu, B., P. Jonsson and M. J. Cervantes (2012). Experimental investigation of a Kaplan draft tube - Part I: Best efficiency point. *Applied Energy* 93,695-706.

Pinto, R.N., A. Afzal and L.V. D'Souza (2016). Computational Fluid Dynamics in Turbomachinery: A Review of State of the Art. *Archives of Computational Methods in Engineering* 1-13.

Smirnov, P. and F. Menter (2009). Sensitization of the SST turbulence model to rotation and curvature by applying the Spalart-Shur correction term. *Journal of Turbomachinery* 131.

Soltani-Dehkharqani, A., K. Amiri and M. J. Cervantes (2015). Steady and transient pressure measurements on the runner blades of a Kaplan turbine model. *Proceedings of the 6th IAHR meeting of the Working Group on Cavitation and Dynamic Problems*, Ljubljana, Slovenia.

Trivedi, C., M. J. Cervantes and O. G. Dahlhaug

(2016). Numerical Techniques Applied to Hydraulic Turbines: a Perspective Review. *Applied Mechanics Reviews* 68(1).

Wilheim, S. (2016). *Étude des pertes de charge dans un aspirateur de turbine bulbe par simulations numériques instationnaires*. Ph.D. thesis, Grenoble Institude of Technology, Grenoble, France.

Wu, H., J. J. Feng, G. K. Wu and X. Q. Luo (2012). Numerical investigation of hub clearance flow in a Kaplan turbine. *IOP Conference Series: Earth and Environmental Science* 15.

Wu, Y., S. Liu, H-S. Dou, S. Wu and T. Chen (2011). Numerical prediction and similarity study of pressure fluctuation in a prototype Kaplan turbine and the model turbine. *Computers & Fluids* 56,128–142.

Wylie, E.B. and V.L. Streeter (1993). *Fluid Transients in Systems*. Prentice Hall, Englewood Cliffs, New Jersey, USA.

Zhou, L., Z. Wang, R. Xiao and Y. Luo (2007). Analysis of dynamic stresses in Kaplan turbine blades. *Engineering Computations* 24(8), 753 – 762.